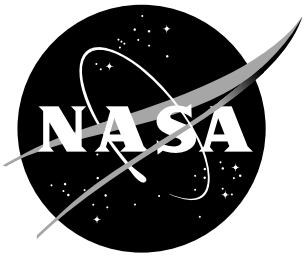

NASA Technical Memorandum 108542

Testing for Random Limit Load Versus Static Limit Load

H.M. Lee

September 1997

NASA Technical Memorandum 108542

Testing for Random Limit Load Versus Static Limit Load

H.M. Lee
Marshall Space Flight Center • MSFC, Alabama

National Aeronautics and Space Administration
Marshall Space Flight Center • MSFC, Alabama 35812

September 1997

TABLE OF CONTENTS

LIST OF ILLUSTRATIONS

LIST OF TABLES

TECHNICAL MEMORANDUM

TESTING FOR RANDOM LIMIT LOAD VERSUS STATIC LIMIT LOAD

INTRODUCTION

The present philosophy[1] for space flight hardware involves the calculation of random load factors based on (1) analytical or tested values for significant resonant frequency (f_n), (2) a conservative, historically based damping value of 5 percent (Q = 10) or component measured damping during testing, (3) the maximum input flight environment at resonance (PSD_n), and (4) a statistically 3σ definition of peak load:

$$G_{pk} = 3\sqrt{\frac{\pi}{2} \times Q \times f_n \times PSD_n} \quad .$$

Combining this, where appropriate, with transient low-frequency/quasi-static loads, then constitutes the limit dynamic loads used in both strength assessments and any static strength qualification or acceptance test. It is assumed that the random and deterministic loads can be superimposed. Thus, the current approach to loads and subsequent hardware strength evaluation effectively equates the limit dynamic load (stress) to the limit static load (stress).

A study completed in 1993 by the Marshall Space Flight Center (MSFC) Random Loads/Criteria Issues Team concluded, after an extensive literature search, that almost no analytical or empirical documentation exists on the subject of the relationship between random limit load (stress) and static limit load (stress). The consensus of the team was that it is a complex subject and requires a carefully planned effort to produce an effective, yet practical, solution. In addition, no amount of analysis or planning will ever completely solve the problem of the dynamic-to-static limit load relationship. It is paramount that ample validation testing be accomplished so a database of hardware response can be built.

The Atmospheric Emission Photometric Imaging (AEPI) experiment (see fig. 1) fiberglass pedestal structure quickly became a good candidate for this early investigation, as it had been previously subjected to static strength acceptance tests prior to flights on the Spacelab–1 and ATLAS–1 Shuttle missions. The component, too, had been slated for retirement from service and thus was made available for the proposed testing. The original static tests were accomplished using strain gauge instrumentation all around the base of the fiberglass pedestal and a complement of deflection gauges. The results of these static tests are documented in reference 2. The key approach presented herein is simply to effect a comparison of strains and associated stresses between the previously run static tests and proposed random environment tests. In both cases the hardware would have identical instrumentation.

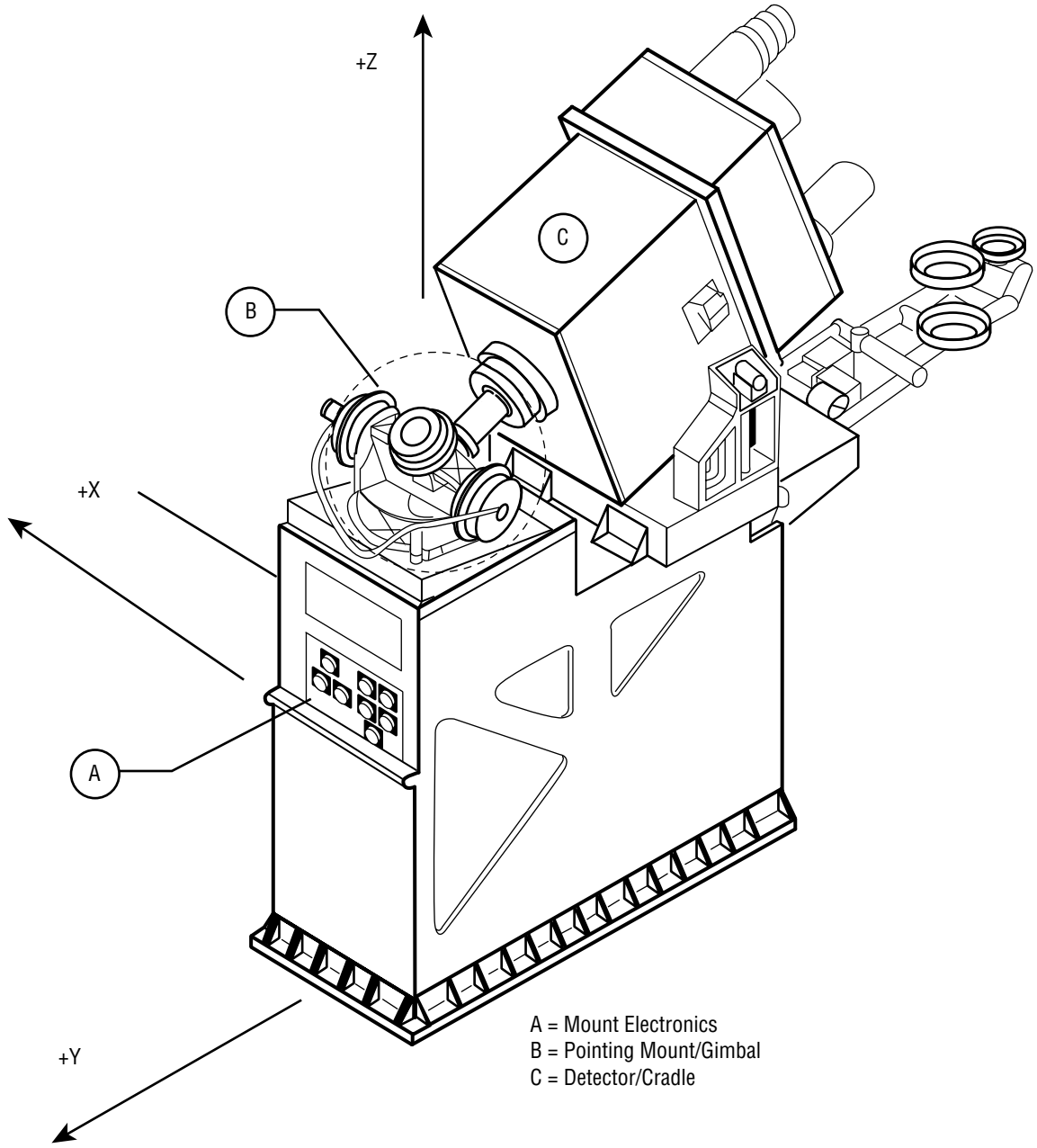

FIGURE 1.—AEPI fiberglass pedestal.

DETERMINATION OF LOADS

The random environment for the AEPI experiment is shown in table 1 below. This loading is derived from the "Spacelab Payload Accommodations Handbook (SPAH)"[3] and relates to components mounted on the orthogrid structure for the ATLAS–1 mission. Such was the case for the AEPI.

TABLE 1.—*X-axis random vibration environment for AEPI.*

Direction	Frequency (Hz)	PSD Level
X-axis	20–82	0.006 g^2/Hz
	82–150	+6 dB/oct
	150–350	0.02 g^2/Hz
	350–2,000	–7 dB/oct
	2,000	0.00034 g^2/Hz
		3.2 grms

From both dynamic analysis and test of the AEPI, the Component Assessment Branch (ED23) of MSFC determined that the random loading factor in the X-axis was:

$$\pm 5.04\ \text{g} \equiv \left(3\sqrt{\frac{\pi}{2} \times 30\ \text{Hz} \times 0.006\ \text{g}^2/\text{Hz} \times 10} \right)\ .^4$$

The key at this point was to now develop the equivalent X-axis acceleration load factor present during the static testing of the same hardware. Table 2 depicts the forces and moments developed at the base of the fiberglass pedestal for two typical static load cases. Reference 2 contains a detailed breakdown of the weights and centroids for the complete experiment package in the flight configuration.

TABLE 2.—*Static test loads for AEPI.*

Case	F_x	F_y (lb)	F_z	M_x	M_y (in-lb)	M_z
2(+++)	4,164	838	956	–37,604	165,355	27,916
5(+ – –)	4,164	–838	–956	37,604	165,245	27,480
$\sum \frac{(\text{case 2} + \text{case 5})}{2.0}$	4,164	0	0	0	165,800	26,480

If results from data such as case 2 and case 5 are added together and divided by 2.0, an X-axis only loading appears. In this manner strains and stresses were later extracted from the static test data to compare with X-axis random vibration strains and stresses.

As can be seen from figure 1, three major mass items are associated with the AEPI pedestal: electronics box (A), gimbal point (B), and detector (C). Static loading of the pedestal was effected through rigid test brackets which interfaced where these items attach to the pedestal. Table 3 shows the actual loads applied to the structure at these three locations in order to obtain the forces and moments desired from table 2.

TABLE 3.—*Actual static test loads for AEPI on ATLAS–1 mission.*

Load Point	Axis	Case 2	Case 5	$\sum \frac{(\text{case 2} + \text{case 5})}{2.0}$
Electronics Box (A)	x	496	496	496
	y	119	–119	0
	z	151	–151	0
Gimbal Mount (B)	x	676	676	676
	y	169	–169	0
	z	189	–189	0
Detector (C)	x	2,992	2,992	2,992
	y	550	–550	0
	z	616	–616	0

Utilizing the loading point dimensions shown in figure 2, the effective static acceleration in the X-axis can be calculated by the following:

force and moment check

$$\sum F_x = 496 + 676 + 2{,}992 = 4{,}164 \text{ lb}$$

$$\sum M_y = 496(25.13) + 676(40.59) + 2{,}992(42.07) = 165{,}750 \text{ in-lb.}$$

Assuming a single mass point of 4,164 lb, the overall centroid can be calculated

$$4{,}164\,(\bar{z}) = 165{,}750$$

$$\bar{z} = 39.80 \text{ in} \quad .$$

The equivalent static acceleration $G_{x\ static}$ is found as

$$(\bar{z})\,(W_{AEPI})\,(G_{x\ static}) = 165{,}750$$

$$G_{x\ static} = \frac{165{,}750}{(39.80)\ (368.74)} = 11.3 \text{ g} \quad .$$

In order to compare the static test results with those from the predicted flight vibration environment, all static data was multiplied by 0.446 (5.04/11.3).

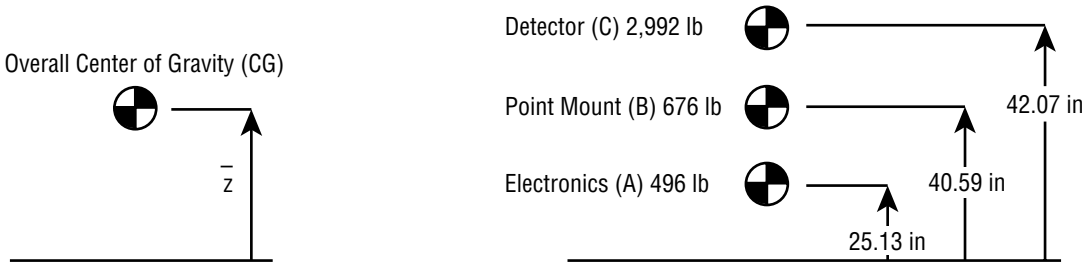

FIGURE 2.—AEPI static load point locations.

For vibration testing, the AEPI experiment was hard mounted to a lateral shake table, resulting in excitation in the X-axis. In each phase of testing the resulting accelerations and associated strains were recorded. The random vibration testing was sequenced in the following way:

Phase I: **Diagnostic Checkout (X-Axis)**

A low level sinusoidal sweep of 0.25 g peak from 5 Hz to 2,000 Hz at 2.0 octaves per minute. The first natural frequency was about 30 Hz.

Phase II: **ATLAS–1 Mission (X-Axis)**

The AEPI was subjected to the expected X-axis random flight level for the ATLAS–1 mission as shown in table 1 (3.2 grms).

Phase III: **ATLAS–1 Mission +3 dB (X-Axis)**

The AEPI was subjected to the expected X-axis random flight level for the ATLAS–1 mission +3 dB (4.5 grms).

Phase IV: **White Noise Spectrum (X-Axis)**

The AEPI was subjected to a flat spectrum random environment of 0.012 g^2/Hz across a frequency range from 20 to 2,000 Hz. This magnitude represents +3 dB above the ATLAS–1 level for the first natural frequency.

Phase V: **Narrow Band Excitation (X-Axis)**

The AEPI was subjected to a flat spectrum random environment of 0.012 g^2/Hz across a narrow bandwidth from 10 to 50 Hz encompassing only the first mode. Again, this magnitude represents +3 dB above the ATLAS–1 level for the first natural frequency.

TEST INSTRUMENTATION

The strain gauge instrumentation of interest consisted of 16 rosettes (triaxials) mounted to the base of the fiberglass pedestal and depicted in figures 3 through 6. The locations of these gauges during the random vibration tests were identical to those utilized in the prior static strength acceptance tests. While the random tests had seven additional channels of accelerometer data (fig. 7), the static test had numerous deflection gauges and nine load cells. It should be noted here that extreme care must be taken in applying and removing gauges from critical flight hardware so no surfaces are damaged.

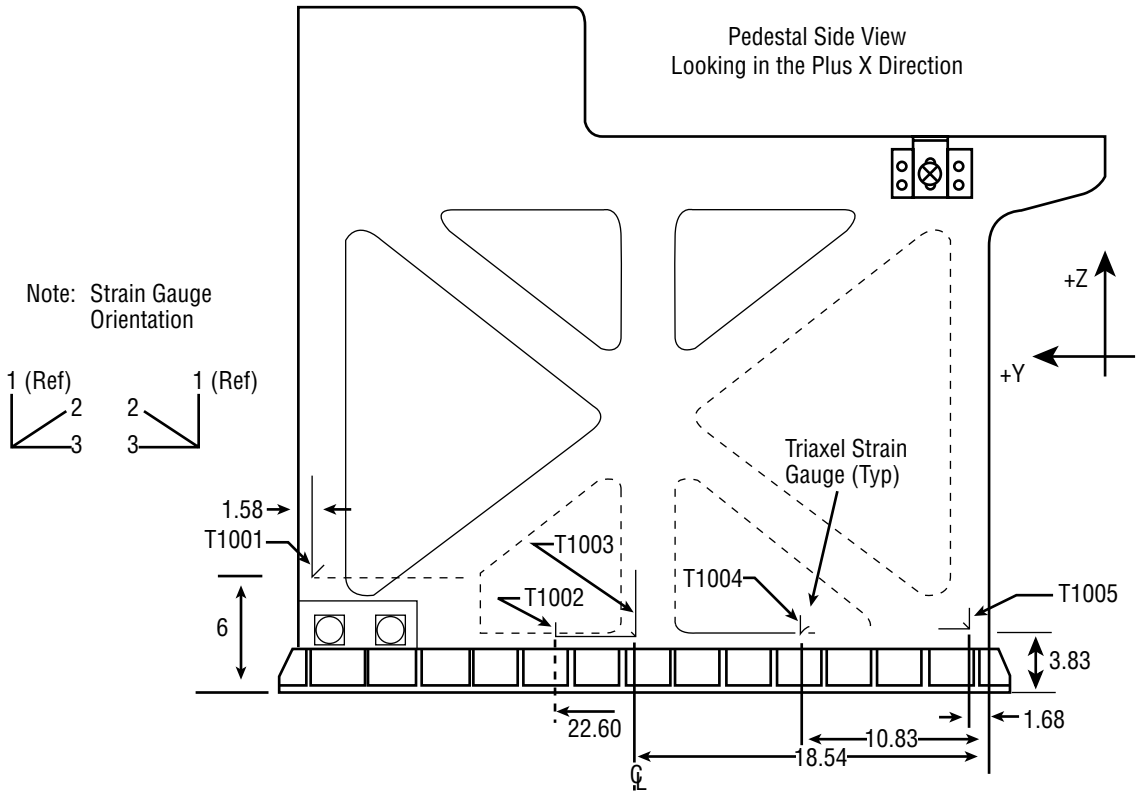

Note: All dimensions are inches

FIGURE 3.—Pedestal strain gauge instrumentation –X side.

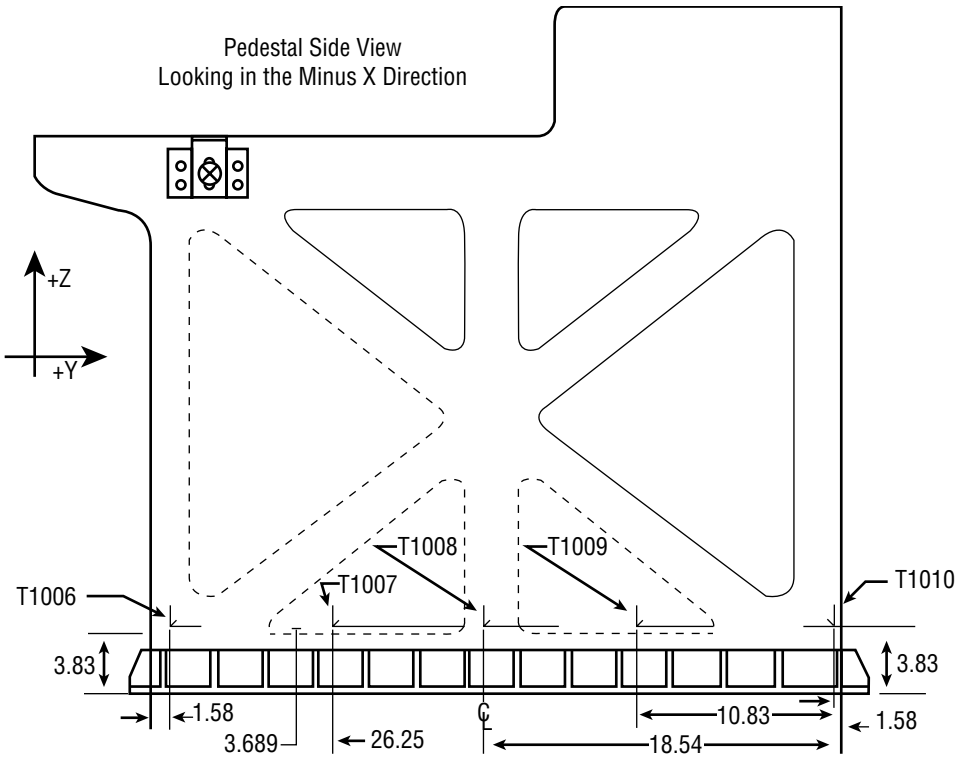

Note: All dimensions are inches

FIGURE 4.—Pedestal strain gauge instrumentation +X side.

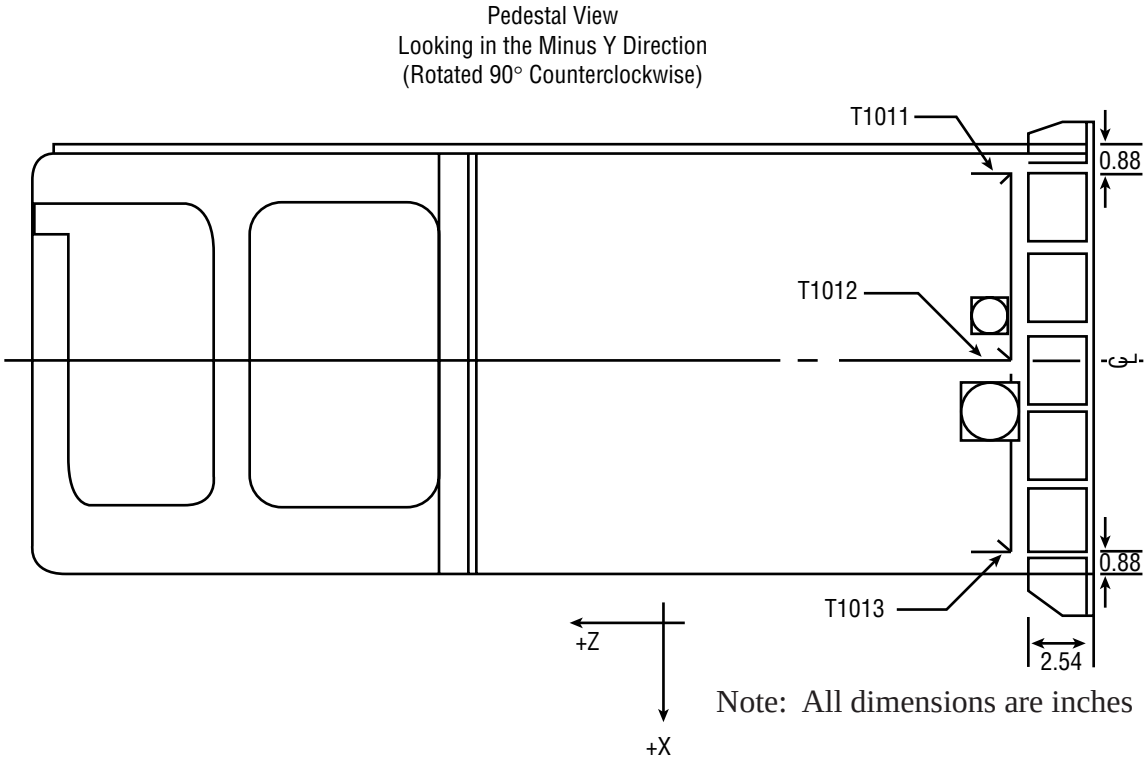

Note: All dimensions are inches

FIGURE 5.—Pedestal strain gauge instrumentation +Y side.

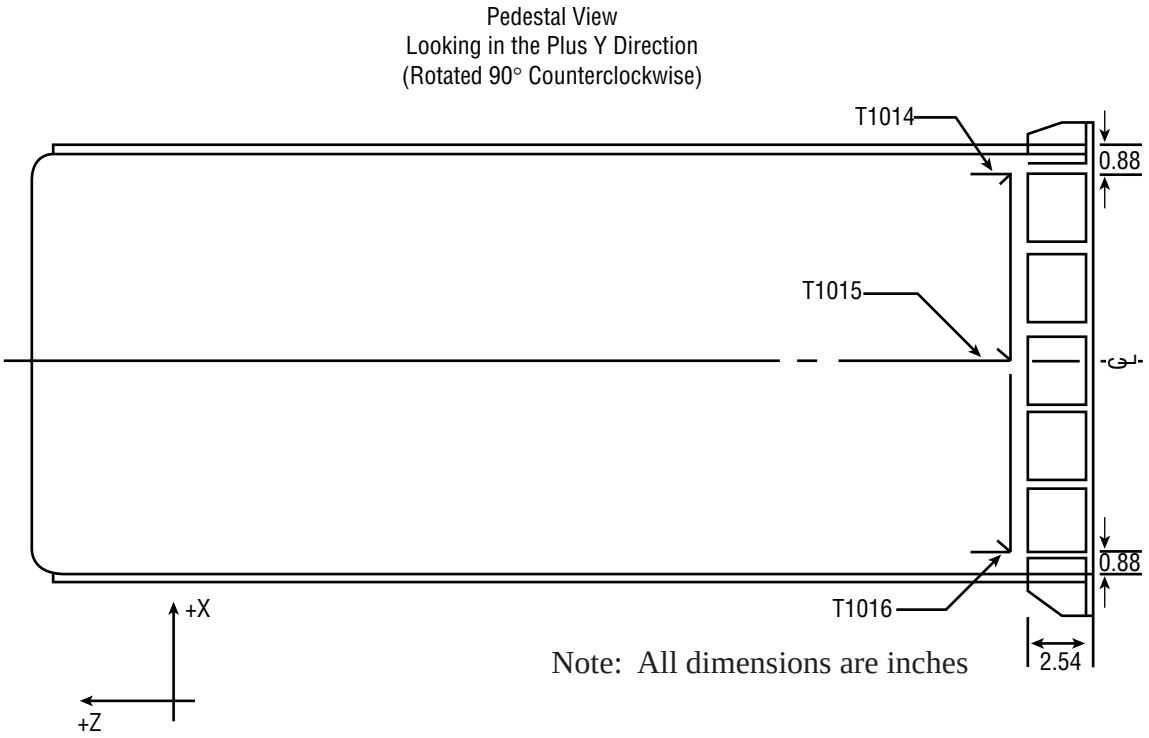

FIGURE 6.—Pedestal strain gauge instrumentation –Y side.

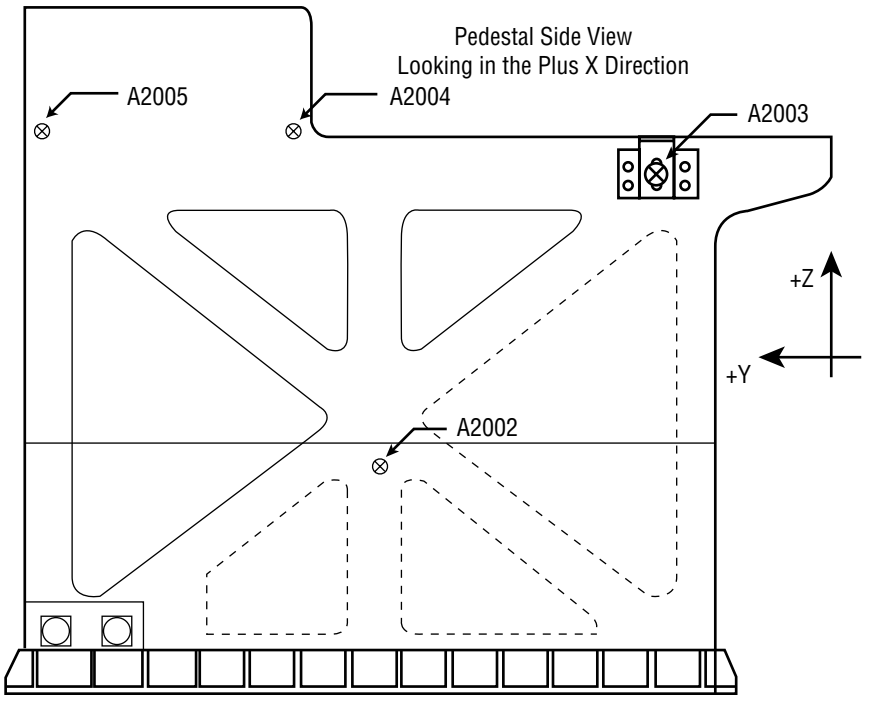

FIGURE 7.—Pedestal accelerometer locations.

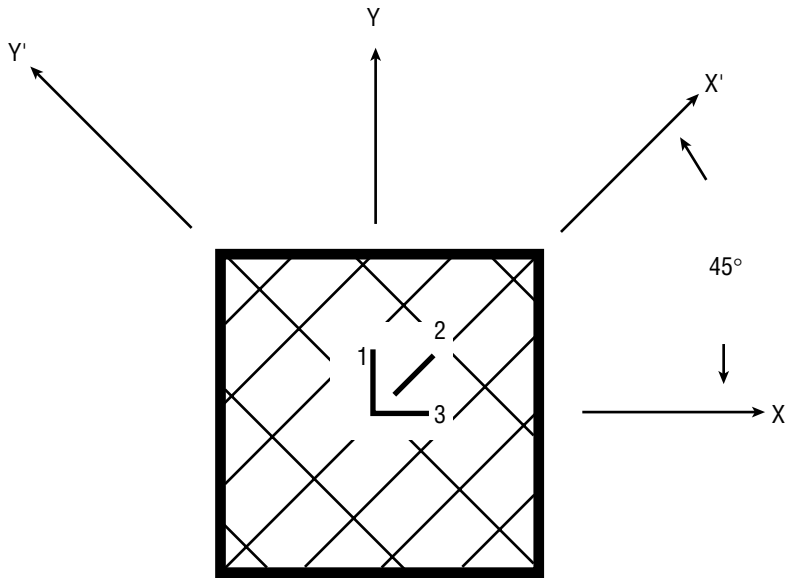

(±45 Lay-up)

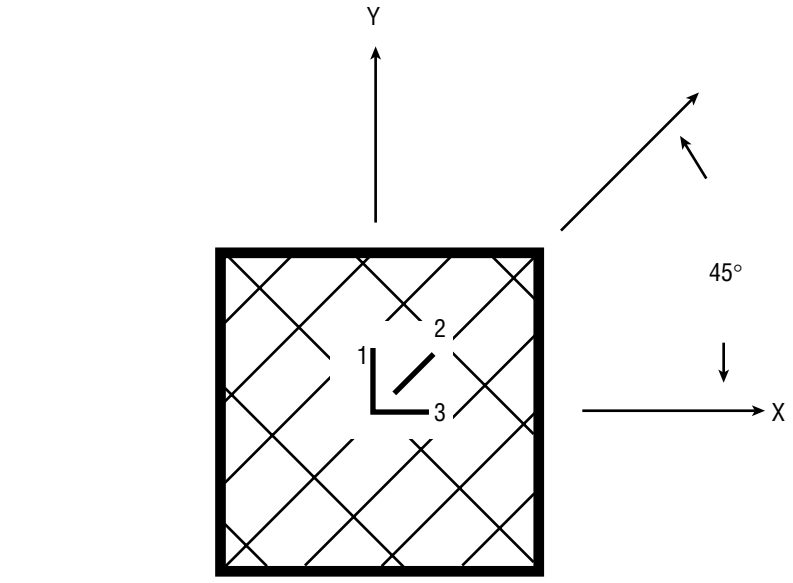

(0, 90 Lay-up)

FIGURE 8.—Strain gauge to panel lay-up relationship.

STATIC/RANDOM STRAINS

Each strain gauge rosette has three legs on the instrument. For gauges T1001 through T1010, the relationship between the three legs of the gauges and the fiberglass panels (±45 degree lay-up) is shown in figure 8. Using matrix transformation,[2] the actual stresses resulting from the load induced strains can be calculated as:

$$\sigma_x = 1.9295\varepsilon_1 - 0.0569\varepsilon_2 + 1.4795\varepsilon_3$$

$$\sigma_y = 1.4795\varepsilon_1 - 0.0569\varepsilon_2 + 1.9295\varepsilon_3$$

$$\tau_{xy} = -1.3393\varepsilon_1 + 2.6339\varepsilon_2 - 1.3393\varepsilon_3 \ .$$

For gauges T1011 through T1016, the relationship with the panel (0, 90 degree lay-up) also is shown in figure 8. The equation for resolving stress at these locations is:

$$\sigma_x = 0.3652\varepsilon_1 + 2.9423\varepsilon_3$$

$$\sigma_y = 3.0438\varepsilon_1 + 0.3530\varepsilon_3$$

$$\tau_{xy} = 0.45\left[\left(\frac{\varepsilon_1 + \varepsilon_3}{2}\right) - \varepsilon_2\right] \ .$$

The data utilized in this report were captured and processed by Teledyne Brown Engineering with a portable system[5] developed within their own shop. Briefly, the time capture process is accomplished with an HP3566A format to ASCII so the data can be manipulated by the MCAD 4.0 software system. The strain data acquired from the random vibration test is processed to generate the strain PSD (ε^2/Hz). Figure 9 shows this process in block diagram form while figure 10 is a typical data output from the test.

Using the process described above, the magnitudes of the three strain legs (ε_1, ε_2, ε_3) have been plotted for each gauge around the pedestal base. Data from each of the four phases of random testing and from the static loading are included in figures 11 through 13. Phases III, IV and V were run at power levels +3 dB above the phase II flight level, so in each of these cases the plot data was divided by $\sqrt{2}$.

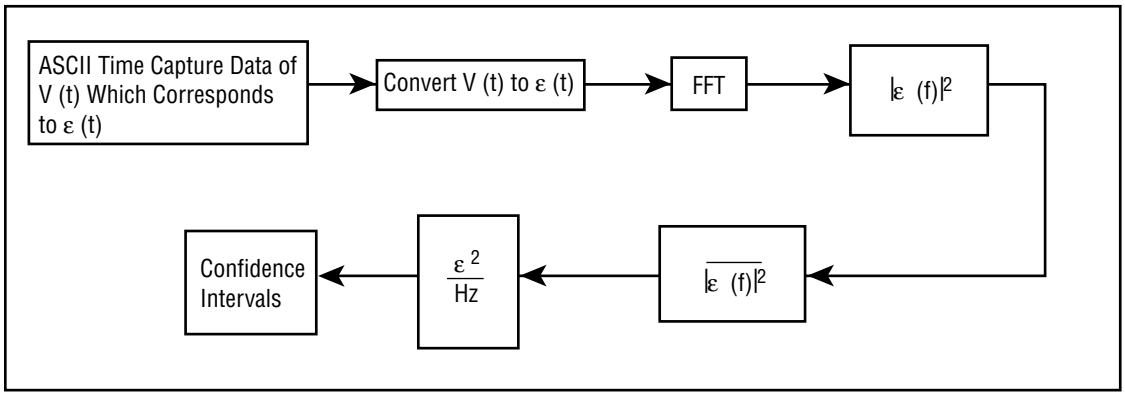

FIGURE 9.—Strain one-sided PSD computational process.

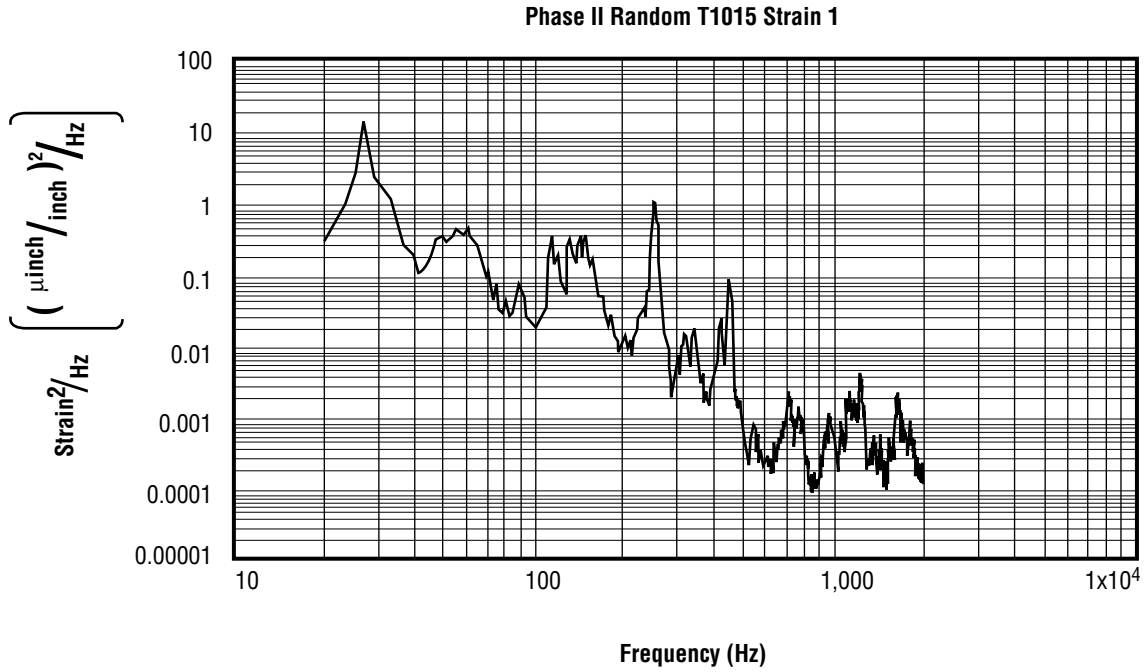

FIGURE 10.—Typical strain PSD plot

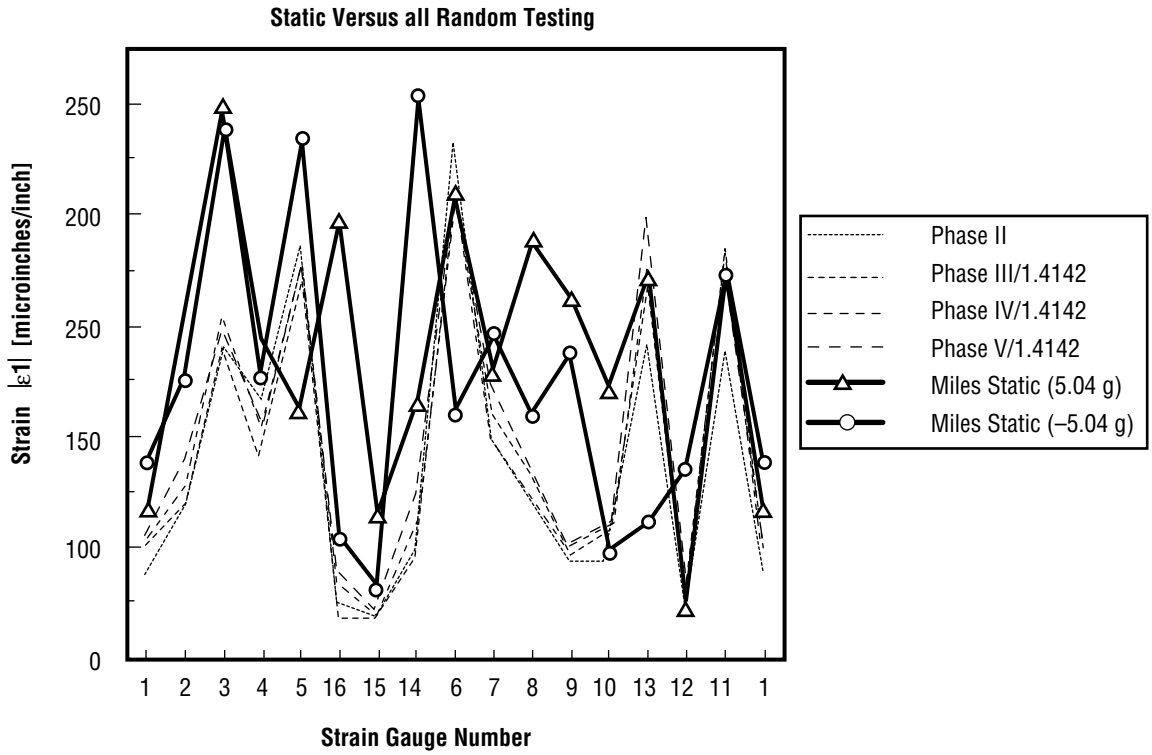

FIGURE 11.—Absolute strain $|\varepsilon_1|$.

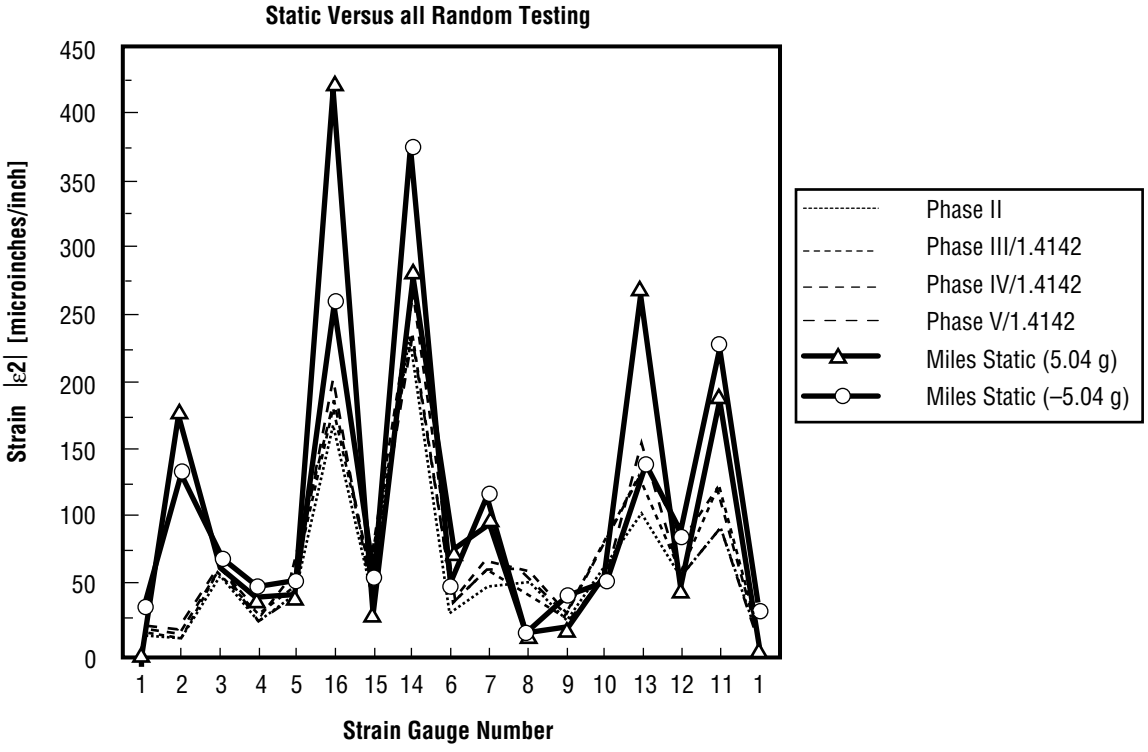

FIGURE 12.—Absolute strain $|\varepsilon_2|$.

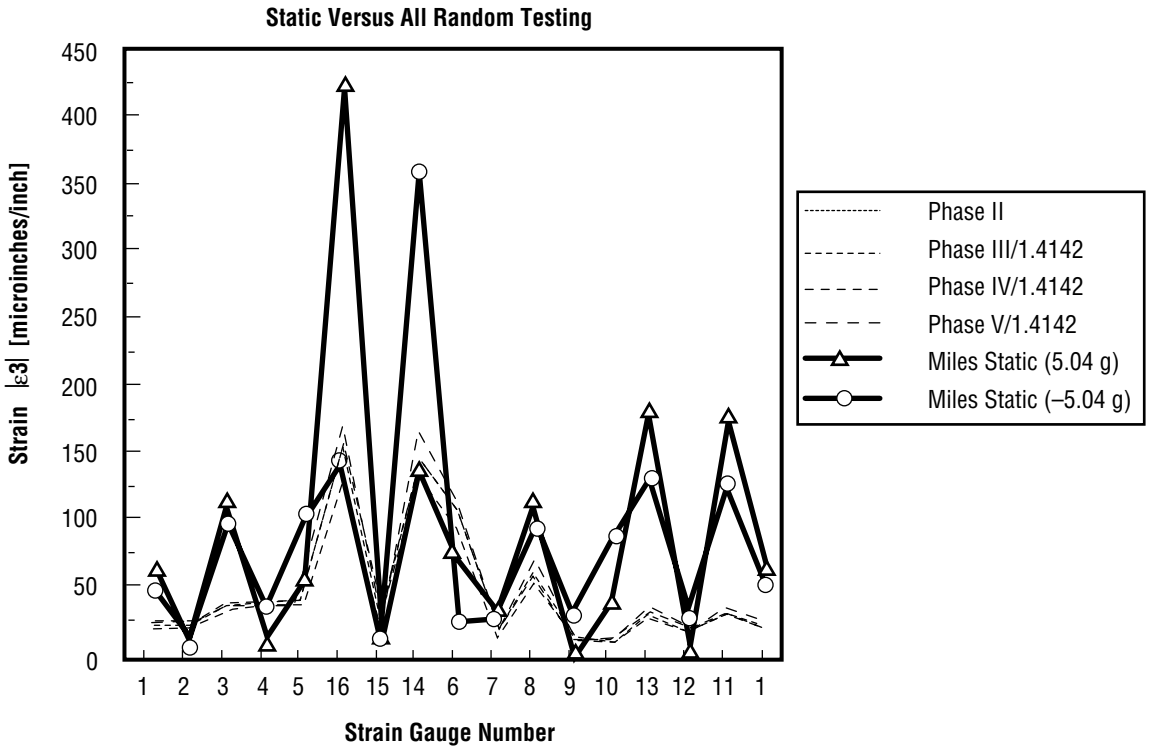

FIGURE 13.—Absolute strain $|\varepsilon_3|$.

STATIC/RANDOM STRESS INVARIANT

The Von Mises stress invariant equation used in this analysis is:

$$\sigma_{inv} = \left(\sigma_x^2 - \sigma_x\sigma_y + \sigma_y^2 + 3\tau_{xy}^2\right)^{\frac{1}{2}} .$$

The component stress values were derived from the equations shown in the previous section for strain gauges T1001 through T1016. Figure 14 again relates how the time domain random vibration rosette strain gauge data is converted to the PSD of the stress invariant $\left(\frac{\sigma_{inv}^2}{\text{Hz}}\right)$ one-sided power spectral density utilizing the Teledyne Brown Engineering HP3566A and MCAD 4.0 system. Figure 15 depicts a typical data output from the test. Once again, data from each of the four phases of random testing and from the static loading cases are plotted for each gauge location around the pedestal. Figures 16 through 19 illustrate each individual random test phase versus the static, while figure 20 captures all random test phase stress invariants versus the static tests. Once again, in these figures the invariant data is divided by $\sqrt{2}$ to account for phases III, IV, and V being +3 dB above the phase II flight levels.

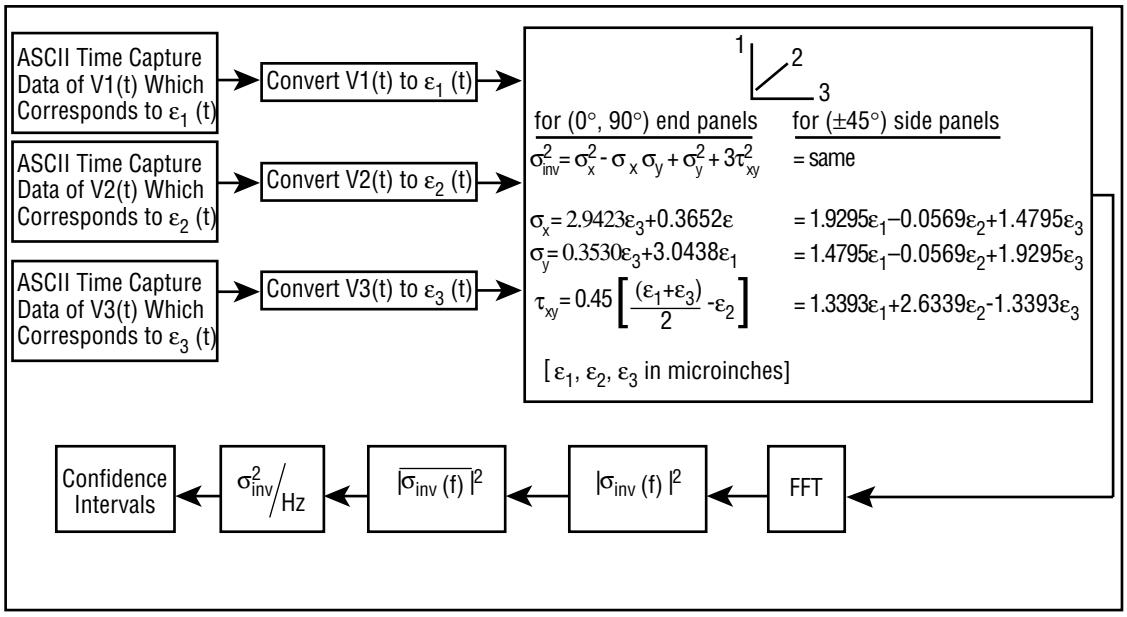

FIGURE 14.—Stress invariant one-sided PSD computational process.

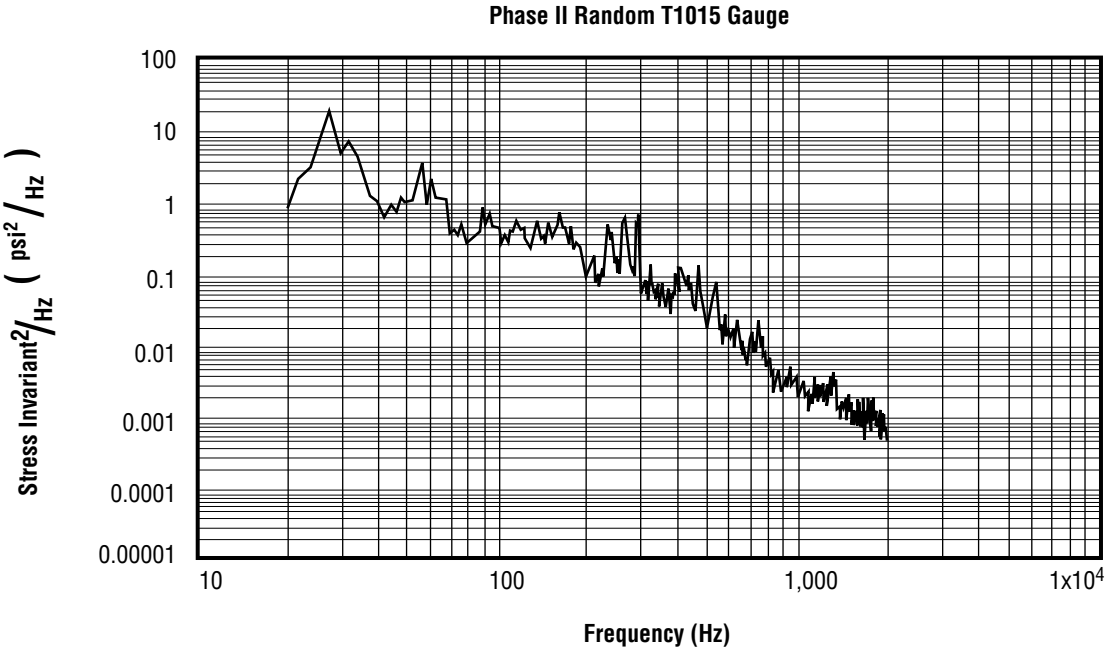

FIGURE 15.—Typical stress invariant PSD plot.

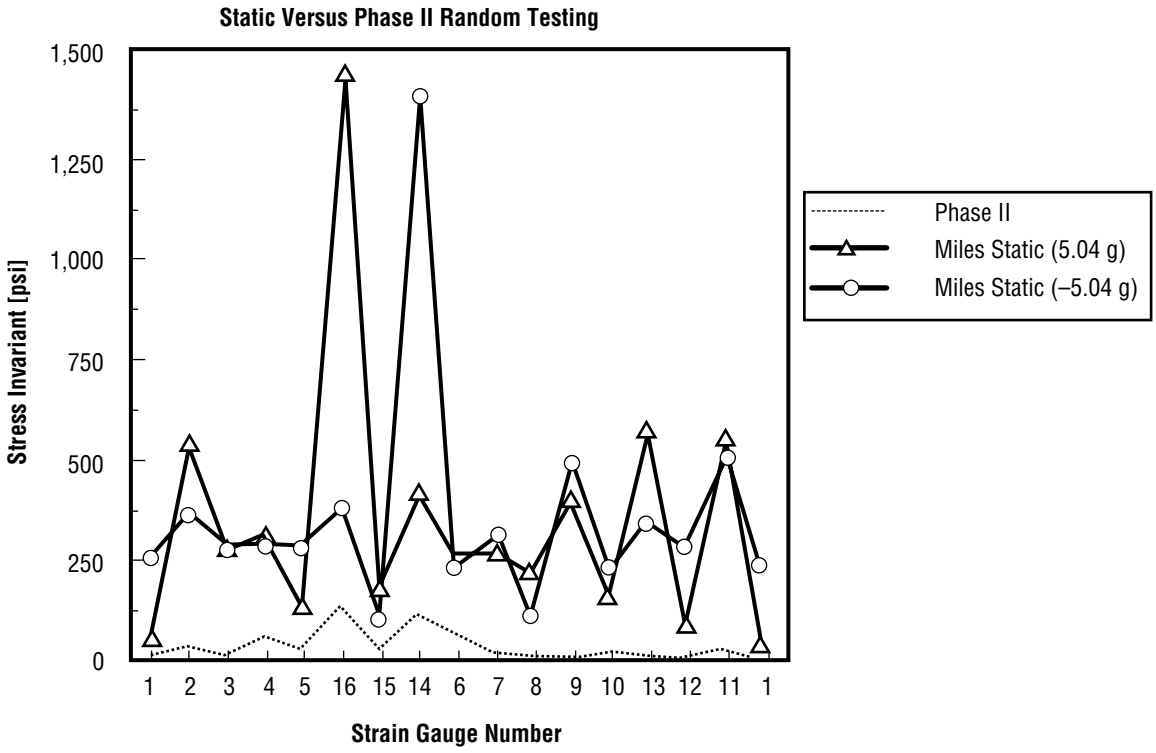

FIGURE 16.—Stress invariants for phase II and static testing.

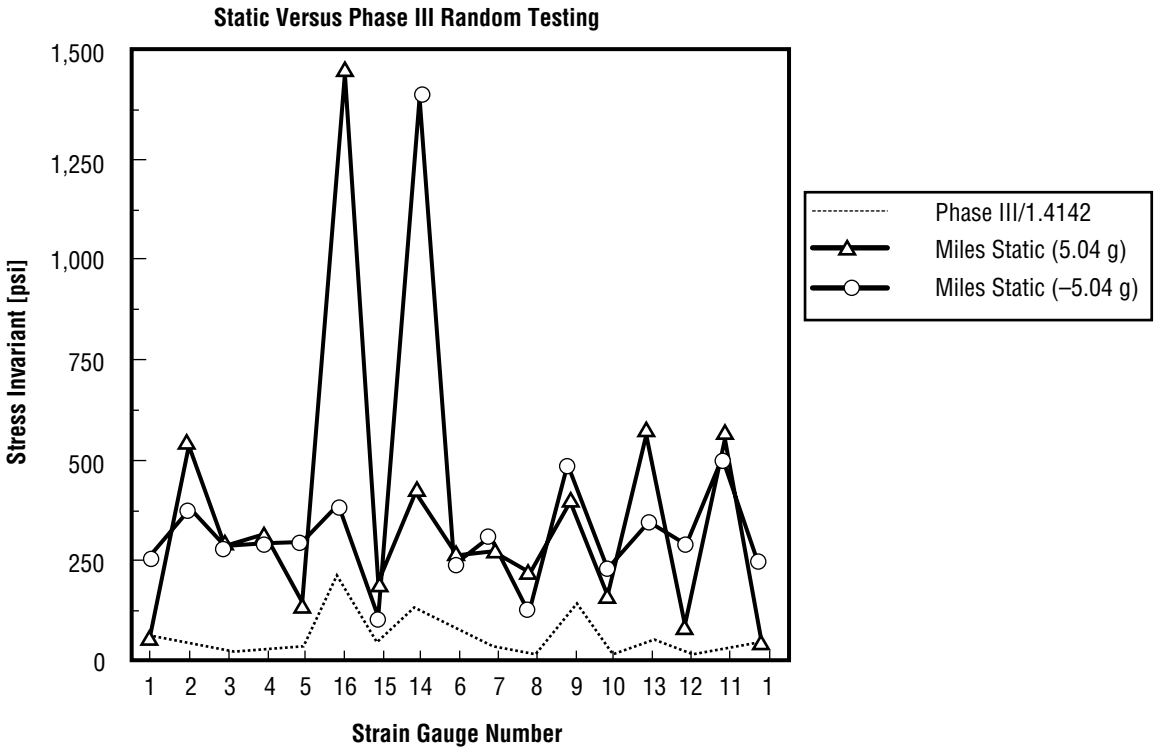

FIGURE 17.—Stress invariants for phase III and static testing.

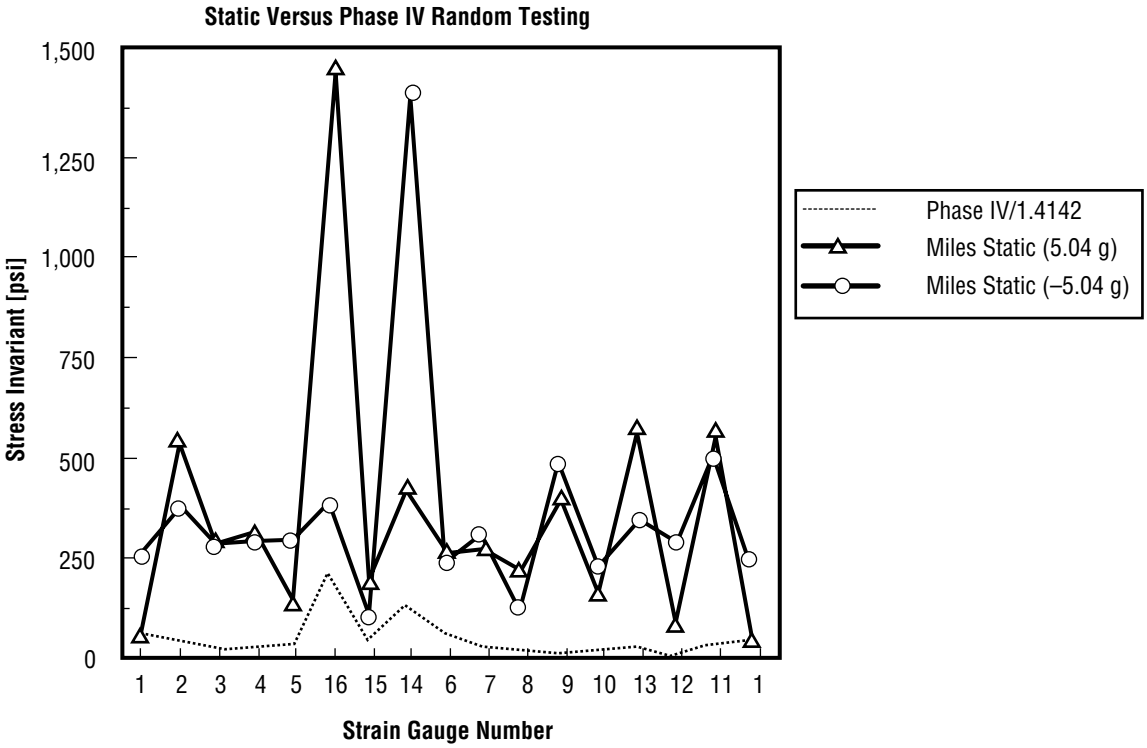

FIGURE 18.—Stress invariants for phase IV and static testing.

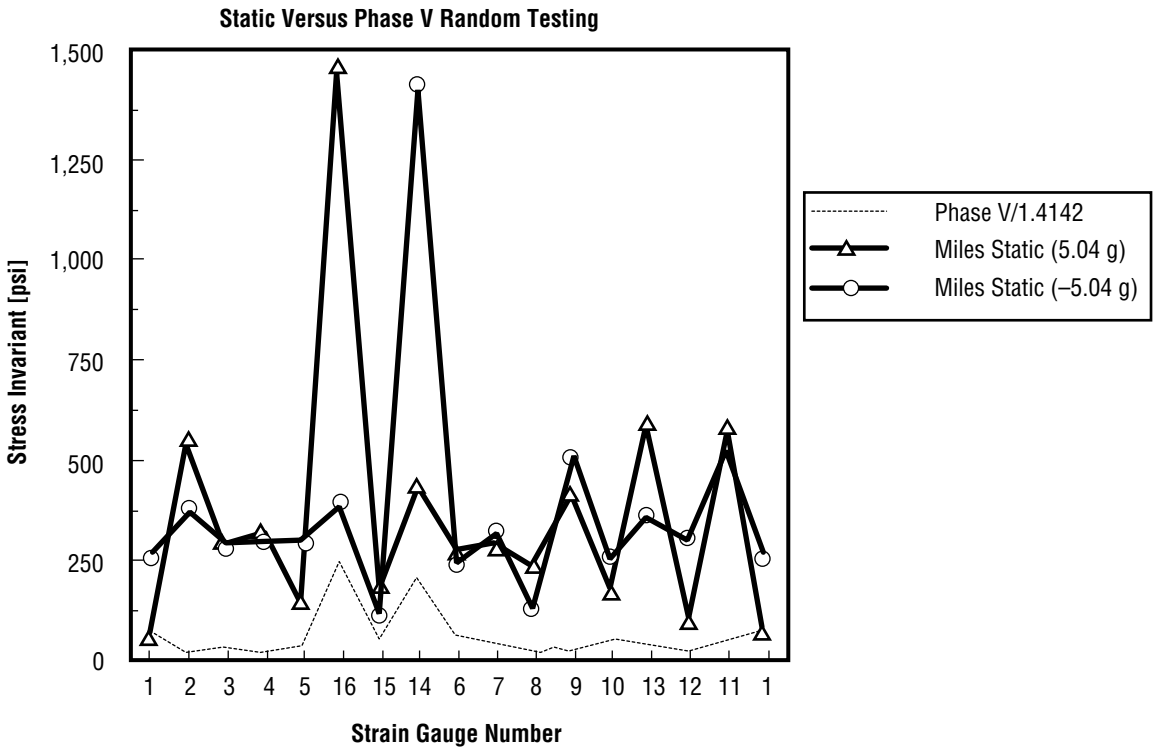

FIGURE 19.—Stress invariants for phase V and static testing.

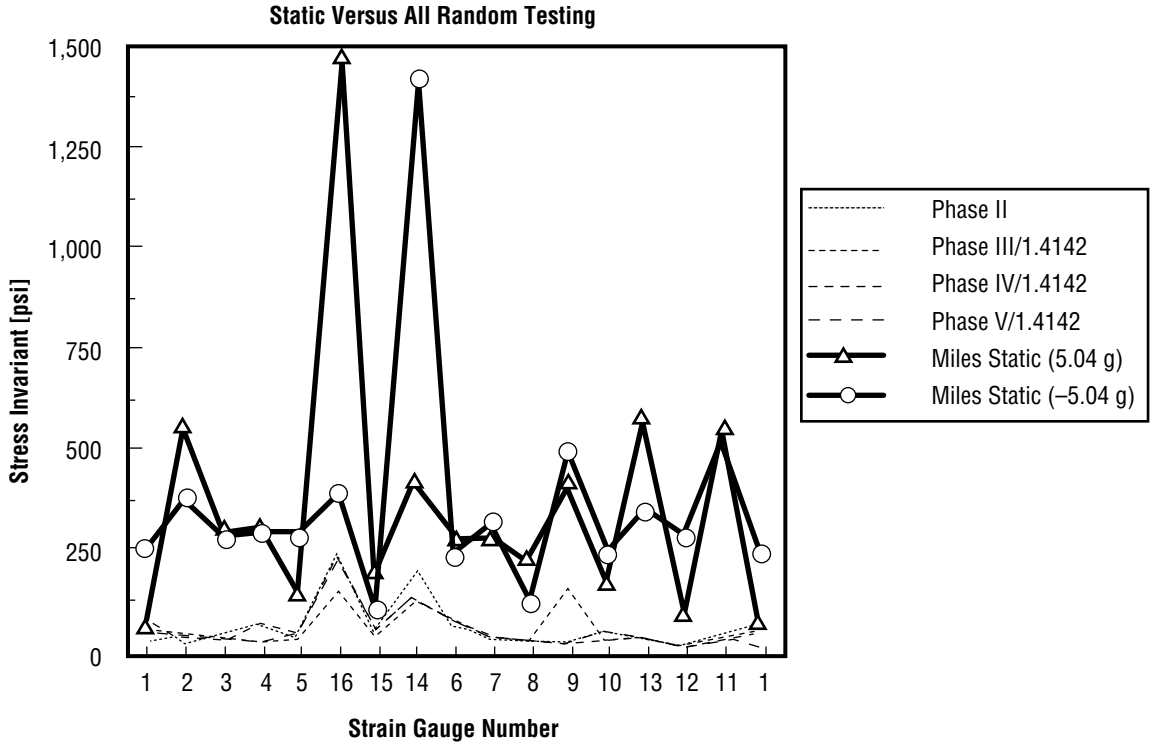

FIGURE 20.—Stress invariants for all random and static testing.

CONCLUSIONS

One of the key findings from this study is that strain, in general, is lower during random testing than during an equivalent static loading as predicted by the Miles' equation. The individual strain components (ε_1, ε_2, ε_3) from the fiberglass pedestal on the AEPI experiment indicate that in the 1-direction, the magnitudes of the random strains measured are about the same as in the static testing. In the 2- and 3-directions, however, the static strains are consistently two to four times higher than the random generated data. Because of the 1-direction strains, a blanket statement cannot be made that the random loading produces lower strain for the composite material. Since most composite allowables are actually strain and direction dependent, the testing is not conclusive enough to say that the random loading will always be less than the static loading. The test implications for a truly isotropic material, however, are that stress would be the principal parameter to review.

As stated previously, the phase II testing was conducted at flight power levels; however, the other test phases were accomplished +3 dB above flight. This means that the data from these phases were divided by $\sqrt{2}$ to compare them directly with the phase II results. There was no discernible difference between the four phases for the strain components measured. This probably indicates that the first mode of the structure in the x-axis was accountable for a majority of the response.

Unlike strain, the stress invariant shows a consistent pattern. The Miles' equation equivalent static loading clearly develops stresses an order of magnitude above those created by the random environments. Hence, for a failure criterion that uses stress components, static loads are much more severe when utilizing a static test. This would certainly be directly applicable to most isotropic metallic components. Similarly, previous testing on other flight components has solidified this fact.

We currently are acquiring a stand-alone data/computational system capable of measuring 60 channels of strains and accelerations during ground testing of flight hardware. This measurement system will enable the strength and dynamics personnel to develop the strain database necessary to quantify the actual stress magnitudes from expected flight transient and random environments. In the short term, these data can potentially affect the rationale for strength margins of safety where random load factors are a major contributor to low or negative margins. The acquisition system also will enable the analysts to verify strength finite element models of hardware subjected to sine burst testing. The only point of concern here will be the application and removal of strain gauges to critical flight hardware. Techniques must be developed where even fracture-critical components are not at risk to surface damage. In the long term, a permanent working relationship between dynamic and static limit stresses can be developed for many space flight components and experiments. This knowledge, based on empirical experience, will allow engineers to more efficiently design flight structures and significantly affect the more weight-critical missions. Potential tasks such as the Next Generation Space Telescope may have a mirror 25 feet in diameter and weigh less than 2,200 pounds, enabling its placement into the desired orbit. A more accurate estimate of the launch environment will be needed so that new technology structure is properly fabricated to meet the demands of science and space flight.

REFERENCES

1. Lee, H.M.: “A Simplistic Look at Limit Stresses From Random Loading.” NASA TM–108427, October 1993.

2. Lee, H.M.: “Test and Model Correlation of the Atmospheric Emission Photometric Imaging Fiberglass Pedestal.” NASA TM–103525, October 1990.

3. “Spacelab Payloads Accommodations Handbook (SPAH),” Main Volume, Section 5.

4. MSFC letter ED23–88–139: “ATLAS–1 Vibration and Acoustic Criteria.” October 1988.

5. Teledyne Brown Engineering: “Vacuum System 2.5 Inch Tube, Flange, and Coupler Development Vibration Test Data Report.” 220RPT0928, May 30, 1994.

APPENDIX

RAW DATA

The data in this appendix are taken from the actual response frequency domain plots produced by the measurement system from 20 to 40 Hz. These raw data were then multiplied by the factor 9.0×10^{12} to convert strains to 3σ peak microinch per inch units. The next step was to calculate the actual peak strains and stresses using the frequency bandwidth determined at the half power point. This technique is represented graphically in figure A–1.

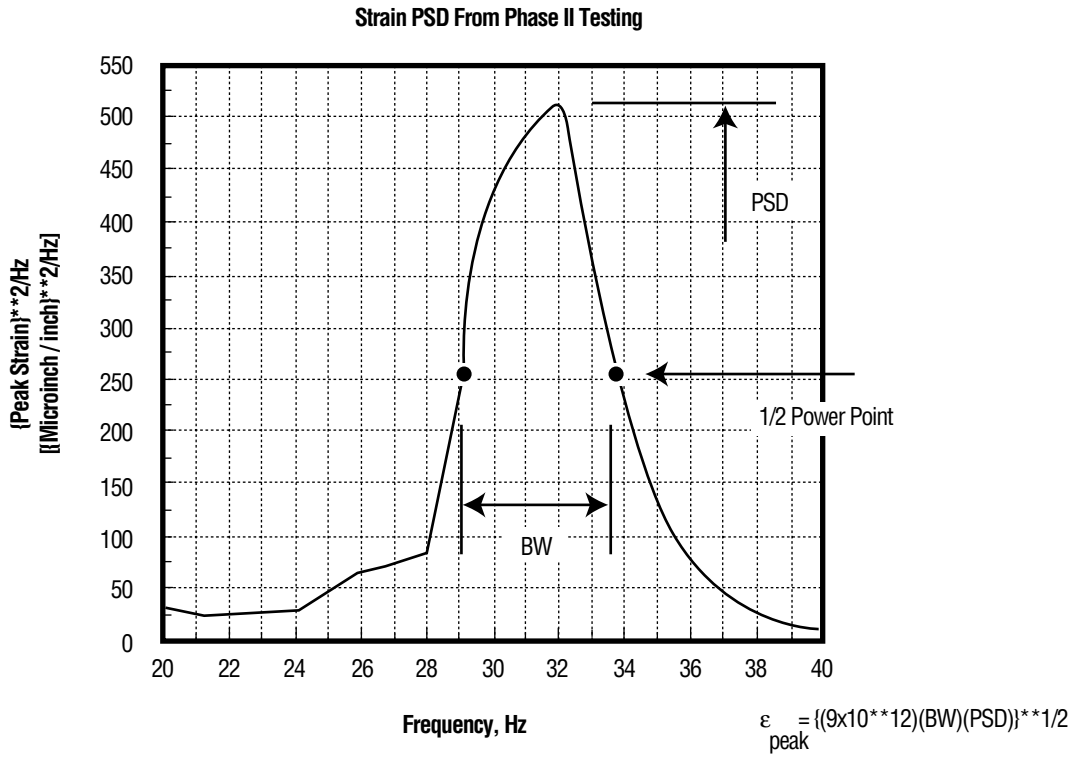

FIGURE A–1.—Peak response determination for raw data.

Phase II Testing

Gauge	Channel	Peak PSD_1	Peak PSD_2	BW_1	BW_2	3σ Peak*
1001	ε_1	510	—	4.7	—	49 με
	ε_2	65	—	2.3	—	12 με
	ε_3	63	—	4.3	—	17 με
	inv	16	10	3.5	4.0	10 psi
1002	ε_1	830	—	5.5	—	68
	ε_2	19	—	3.5	—	8
	ε_3	61	—	2.7	—	13
	inv	153	—	5.7	—	30
1003	ε_1	3,800	—	5.2	—	141
	ε_2	580	—	5.7	—	58
	ε_3	90	190	3.5	3.2	30
	inv	48	38	5.5	4.0	20
1004	ε_1	1,650	2,120	3.4	3.5	114
	ε_2	185	—	3.1	—	24
	ε_3	150	165	3.2	3.6	33
	inv	300	660	4.0	3.5	60
1005	ε_1	5,750	4,200	3.1	4.1	187
	ε_2	290	610	3.5	3.3	55
	ε_3	205	110	2.5	3.8	31
	inv	100	65	3.6	6.5	28
1006	ε_1	8,400	5,500	3.7	4.2	233
	ε_2	100	160	3.5	3.4	30
	ε_3	1,800	1,125	2.8	4.5	100
	inv	400	525	4.0	7.8	75
1007	ε_1	1,420	2,100	3.5	3.2	108
	ε_2	420	900	3.5	3.2	66
	ε_3	8.8	—	4.0	—	6
	inv	225	—	3.1	—	26
1008	ε_1	880	1,300	3.2	3.1	83
	ε_2	450	520	3.0	3.6	57
	ε_3	290	600	3.5	3.3	55
	inv	20	27	4.0	7.0	16
1009	ε_1	310	260	2.8	4.3	45
	ε_2	97	75	2.6	4.5	24
	ε_3	6	—	6.5	—	6
	inv	52	—	5.0	—	16

* 3σ Peak = $\sqrt{(PSD_1 \times BW_1) + (PSD_2 \times BW_2)}$

Phase II Testing (Cont'd)

Gauge	Channel	Peak PSD_1	Peak PSD_2	BW_1	BW_2	3σ Peak*
1010	ε_1	300	600	3.5	3.5	56
	ε_2	500	500	2.5	3.7	56
	ε_3	6.5	—	2.3	—	4
	inv	78	75	4.0	5.0	26
1011	ε_1	3,900	5,250	3.2	4.3	187
	ε_2	1,420	2,650	3.3	4.0	124
	ε_3	75	115	3.3	3.4	25
	inv	375	—	3.0	—	34
1012	ε_1	125	—	2.9	—	19
	ε_2	790	—	3.0	—	49
	ε_3	27	—	3.2	—	9
	inv	37	—	3.6	—	12
1013	ε_1	2,600	6,800	3.2	3.4	177
	ε_2	1,350	3,800	3.3	3.0	126
	ε_3	56	134	4.0	3.3	26
	inv	240	—	3.0	—	27
1014	ε_1	285	200	3.3	5.0	44
	ε_2	8,000	—	7.0	—	237
	ε_3	2,250	1,960	4.0	4.2	131
	inv	1,600	—	8.8	—	119
1015	ε_1	130	—	2.5	—	18
	ε_2	560	—	2.9	—	40
	ε_3	12.5	—	6.7	—	9
	inv	290	—	2.8	—	29
1016	ε_1	62	27	2.8	5.2	18
	ε_2	5,000	2,750	3.3	4.8	172
	ε_3	2,000	1,800	3.5	4.2	121
	inv	3,300	2,750	3.0	4.3	144

* 3σ Peak = $\sqrt{\left(PSD_1 \times BW_1\right) + \left(PSD_2 \times BW_2\right)}$

Phase III Testing

Gauge	Channel	Peak PSD_1	Peak PSD_2	BW_1	BW_2	3σ Peak*
1001	ε_1	920	—	3.0	—	53 με
	ε_2	57	—	4.8	—	17 με
	ε_3	108	—	3.0	—	18 με
	inv	1,190	—	2.8	—	58 psi
1002	ε_1	1,150	1,400	3.3	3.8	96
	ε_2	24	—	6.8	—	13
	ε_3	105	48	3.3	4.0	23
	inv	115	135	6.0	4.5	36
1003	ε_1	4,200	7,400	3.5	3.2	196
	ε_2	800	1,100	3.4	3.3	80
	ε_3	510	—	3.2	—	40
	inv	106	88	4.0	6.0	31
1004	ε_1	5,200	—	3.1	—	127
	ε_2	152	128	4.5	4.0	35
	ε_3	375	—	3.3	—	35
	inv	98	73	3.5	4.0	25
1005	ε_1	5,200	10,300	4.8	3.2	241
	ε_2	1,210	—	2.8	—	58
	ε_3	230	370	4.8	3.8	50
	inv	125	—	4.0	—	22
1006	ε_1	13,500	—	6.7	—	300
	ε_2	190	—	6.6	—	35
	ε_3	2,300	1,400	4.0	4.7	126
	inv	1,050	1,600	4.0	3.7	100
1007	ε_1	1,850	2,700	4.8	4.0	140
	ε_2	1,100	—	4.0	—	66
	ε_3	15	—	4.0	—	8
	inv	270	—	5.6	—	39
1008	ε_1	1,050	1,400	5.0	4.3	106
	ε_2	550	580	4.6	4.3	71
	ε_3	740	350	3.7	5.5	68
	inv	53	—	9.0	—	22
1009	ε_1	400	610	4.3	3.0	60
	ε_2	100	112	3.6	3.2	27
	ε_3	11	—	6.0	—	8
	inv	5,750	7,750	4.0	3.1	217
1010	ε_1	1,320	—	2.8	—	61
	ε_2	700	1,250	4.5	2.6	80
	ε_3	11	—	3.4	—	6
	inv	155	62	2.9	3.8	26

* 3σ Peak = $\sqrt{\left(PSD_1 \times BW_1\right) + \left(PSD_2 \times BW_2\right)}$

Phase III Testing (Cont'd)

Gauge	Channel	Peak PSD_1	Peak PSD_2	BW_1	BW_2	3σ Peak*
1011	ε_1	11,200	—	5.8	—	255
	ε_2	5,700	—	2.9	—	129
	ε_3	260	—	6.0	—	40
	inv	250	—	4.0	—	32
1012	ε_1	235	—	2.8	—	26
	ε_2	1,550	—	2.8	—	66
	ε_3	52	—	2.9	—	12
	inv	125	—	3.2	—	20
1013	ε_1	12,750	—	3.2	—	202
	ε_2	7,550	—	2.8	—	145
	ε_3	290	—	3.2	—	30
	inv	350	—	6.0	—	46
1014	ε_1	660	610	3.7	3.9	70
	ε_2	19,550	12,000	3.2	4.0	332
	ε_3	5,400	4,300	2.8	4.0	180
	inv	4,200	—	6.0	—	159
1015	ε_1	260	—	2.3	—	25
	ε_2	1,260	—	2.5	—	56
	ε_3	31	22	3.3	4.0	14
	inv	350	235	2.8	3.9	44
1016	ε_1	260	150	2.4	3.8	35
	ε_2	11,500	6,000	2.5	4.1	231
	ε_3	5,600	4,600	2.9	3.5	180
	inv	7,250	5,900	2.6	3.5	199

* 3σ Peak = $\sqrt{\left(PSD_1 \times BW_1\right) + \left(PSD_2 \times BW_2\right)}$

Phase IV Testing

Gauge	Channel	Peak PSD_1	Peak PSD_2	BW_1	BW_2	3σ Peak*
1001	ε_1	910	—	6.2	—	75
	ε_2	72	—	4.0	—	17
	ε_3	112	—	3.4	—	20
	inv	430	710	4.0	3.5	65
1002	ε_1	1,650	1,380	3.4	4.3	107
	ε_2	32	—	6.1	—	14
	ε_3	140	—	3.0	—	20
	inv	190	210	4.6	4.0	41
1003	ε_1	6,000	7,200	3.4	3.9	220
	ε_2	1,130	1,060	3.5	4.0	90
	ε_3	360	—	3.3	—	35
	inv	230	—	3.5	—	28
1004	ε_1	2,600	3,750	4.0	3.2	150
	ε_2	285	—	2.9	—	29
	ε_3	240	280	3.8	3.3	43
	inv	125	100	3.4	3.6	28
1005	ε_1	9,000	7,200	3.0	3.8	233
	ε_2	900	—	2.8	—	50
	ε_3	410	240	2.6	4.3	46
	inv	180	190	5.6	4.2	42
1006	ε_1	12,750	9,400	3.6	4.2	292
	ε_2	370	—	5.8	—	46
	ε_3	3,510	—	6.6	—	152
	inv	780	—	11.5	—	95
1007	ε_1	3,100	5,200	3.9	3.3	171
	ε_2	2,100	—	3.3	—	83
	ε_3	28	—	3.2	—	10
	inv	580	—	3.2	—	43
1008	ε_1	1,650	2,700	4.0	3.0	121
	ε_2	810	1,020	4.0	3.4	82
	ε_3	1,380	—	6.3	—	93
	inv	124	—	7.5	—	30
1009	ε_1	410	610	4.8	3.3	63
	ε_2	140	180	3.4	3.3	33
	ε_3	12	—	5.9	—	9
	inv	76	—	4.0	—	17
1010	ε_1	1,320	—	2.9	—	62
	ε_2	710	1,200	5.0	2.8	83
	ε_3	11	—	3.5	—	6
	inv	335	—	4.2	—	38

* 3σ Peak = $\sqrt{\left(PSD_1 \times BW_1\right) + \left(PSD_2 \times BW_2\right)}$

Phase IV Testing (Cont'd)

Gauge	Channel	Peak PSD_1	Peak PSD_2	BW_1	BW_2	3σ Peak*
1011	ε_1	11,300	—	3.5	—	199
	ε_2	5,750	—	3.0	—	131
	ε_3	180	275	3.3	3.2	38
	inv	750	—	4.0	—	55
1012	ε_1	240	—	3.0	—	27
	ε_2	1,700	—	3.0	—	71
	ε_3	57	—	3.2	—	14
	inv	28	—	4.6	—	11
1013	ε_1	5,900	13,100	3.5	2.8	239
	ε_2	3,100	7,700	3.5	2.8	180
	ε_3	140	290	3.5	2.8	36
	inv	735	—	4.0	—	54
1014	ε_1	1,230	790	2.7	4.5	83
	ε_2	21,800	—	6.7	—	382
	ε_3	6,000	4,800	4.0	3.5	202
	inv	6,500	5,400	2.7	3.3	188
1015	ε_1	225	—	2.5	—	24
	ε_2	1,250	—	3.0	—	61
	ε_3	34	—	6.6	—	15
	inv	650	600	2.8	2.8	59
1016	ε_1	330	240	4.0	3.7	47
	ε_2	12,100	7,000	3.6	3.6	262
	ε_3	6,100	5,750	4.2	3.6	215
	inv	13,400	13,300	4.1	3.2	312

* 3σ Peak = $\sqrt{(PSD_1 \times BW_1) + (PSD_2 \times BW_2)}$

Phase V Testing

Gauge	Channel	Peak PSD_1	Peak PSD_2	BW_1	BW_2	3σ Peak*
1001	ε_1	2,100	—	2.6	—	74
	ε_2	45	—	4.2	—	14
	ε_3	250	—	2.6	—	25
	inv	3,200	—	2.6	—	91
1002	ε_1	3,500	1,200	2.9	4.5	125
	ε_2	44	—	3.4	—	12
	ε_3	98	125	4.0	3.6	29
	inv	37	—	6.0	—	15
1003	ε_1	16,600	—	2.6	—	208
	ε_2	2,400	—	2.5	—	77
	ε_3	770	—	2.6	—	45
	inv	150	—	6.0	—	30
1004	ε_1	7,400	—	2.8	—	144
	ε_2	210	200	3.5	3.4	37
	ε_3	560	—	2.8	—	39
	inv	35	—	8.0	—	17
1005	ε_1	6,500	13,500	4.0	2.8	252
	ε_2	1,400	—	2.8	—	62
	ε_3	300	500	3.7	2.9	50
	inv	180	325	4.0	3.2	42
1006	ε_1	9,200	18,000	4.0	3.0	301
	ε_2	625	—	2.7	—	41
	ε_3	1,750	4,200	4.2	2.9	140
	inv	520	620	4.0	6.0	76
1007	ε_1	9,000	—	2.8	—	158
	ε_2	3,500	—	2.5	—	93
	ε_3	56	—	2.6	—	12
	inv	800	—	2.5	—	45
1008	ε_1	4,400	—	2.5	—	105
	ε_2	1,700	—	2.6	—	66
	ε_3	2,350	—	2.5	—	77
	inv	135	—	3.5	—	22
1009	ε_1	400	1,250	3.6	2.8	70
	ε_2	120	360	3.7	3.1	39
	ε_3	17	—	4.6	—	9
	inv	140	78	3.3	4.0	28
1010	ε_1	2,400	—	2.8	—	82
	ε_2	625	2,200	3.8	2.7	91
	ε_3	7.6	—	4.3	—	6
	inv	1,120	—	2.8	—	56

* 3σ Peak = $\sqrt{(PSD_1 \times BW_1) + (PSD_2 \times BW_2)}$

Phase V Testing (Cont'd)

Gauge	Channel	Peak PSD_1	Peak PSD_2	BW_1	BW_2	3σ Peak*
1011	ε_1	20,500	—	3.0	—	248
	ε_2	10,200	—	2.8	—	169
	ε_3	680	—	2.8	—	44
	inv	425	—	7.5	—	56
1012	ε_1	550	—	2.6	—	38
	ε_2	3,750	—	2.7	—	101
	ε_3	120	—	2.8	—	18
	inv	110	—	5.0	—	23
1013	ε_1	30,000	—	2.7	—	285
	ε_2	17,200	—	2.8	—	219
	ε_3	700	—	2.6	—	43
	inv	1,050	—	2.8	—	54
1014	ε_1	1,100	2,150	3.3	3.3	103
	ε_2	21,250	23,700	3.4	3.4	391
	ε_3	6,300	9,000	3.4	3.4	228
	inv	8,700	15,800	3.1	3.2	278
1015	ε_1	175	90	2.8	2.8	27
	ε_2	930	—	4.5	—	65
	ε_3	34	—	6.8	—	15
	inv	475	725	3.3	2.8	60
1016	ε_1	400	550	3.3	2.8	53
	ε_2	11,400	12,500	3.6	3.3	287
	ε_3	6,800	11,250	3.4	2.8	234
	inv	14,500	24,100	3.3	2.8	340

* 3σ Peak = $\sqrt{\left(PSD_1 \times BW_1\right) + \left(PSD_2 \times BW_2\right)}$

REPORT DOCUMENTATION PAGE

Form Approved
OMB No. 0704-0188

1. AGENCY USE ONLY *(Leave Blank)*	2. REPORT DATE	3. REPORT TYPE AND DATES COVERED
	September 1997	Technical Memorandum

4. TITLE AND SUBTITLE

Testing for Random Limit Load Versus Static Limit Load

5. FUNDING NUMBERS

6. AUTHORS

H.M. Lee

7. PERFORMING ORGANIZATION NAMES(S) AND ADDRESS(ES)

George C. Marshall Space Flight Center
Marshall Space Flight Center, Alabama 35812

8. PERFORMING ORGANIZATION REPORT NUMBER

9. SPONSORING/MONITORING AGENCY NAME(S) AND ADDRESS(ES)

National Aeronautics and Space Administration
Washington, DC 20546–0001

10. SPONSORING/MONITORING AGENCY REPORT NUMBER

NASA TM–108542

11. SUPPLEMENTARY NOTES

Prepared by the Structures and Dynamics Laboratory, Science and Engineering Directorate

12a. DISTRIBUTION/AVAILABILITY STATEMENT

Unclassified–Unlimited

12b. DISTRIBUTION CODE

13. ABSTRACT *(Maximum 200 words)*

This document is an effort to report the basic test findings in an ongoing quest for understanding how random load factors should be applied to structural components in order to verify the strength of space flight hardware. A Spacelab experiment known as the Atmospheric Emission Photometric Imager (AEPI) was subjected to both an expected flight random environment and the associated Miles' equation equivalent static load. During each of these tests, the fiberglass pedestal was instrumented with 16 triaxial strain gauges around its base. Component strains and invariant stresses were compared. As seen previously in other hardware tests, the stress distribution from the random environment was an order of magnitude below the comparable static stresses. With a proposed data acquisition system, a strain database will be developed that will quantify an empirical relationship between dynamic and static limit stresses. This event will allow a more accurate estimate of launch environment effects on new technology structural components.

14. SUBJECT TERMS

random vibration, strain gauge, limit load

15. NUMBER OF PAGES

36

16. PRICE CODE

NTIS

17. SECURITY CLASSIFICATION OF REPORT	18. SECURITY CLASSIFICATION OF THIS PAGE	19. SECURITY CLASSIFICATION OF ABSTRACT	20. LIMITATION OF ABSTRACT
Unclassified	Unclassified	Unclassified	Unlimited